

Recognition of polar lows in Sentinel-1 SAR images with deep learning

Jakob Grahn*, Filippo Maria Bianchi

Abstract—In this paper, we explore the possibility of detecting polar lows in C-band SAR images by means of deep learning. Specifically, we introduce a novel dataset consisting of Sentinel-1 images labeled as *positive*; representing a maritime mesocyclone, or *negative*; representing a normal sea state. The dataset is constructed using the ERA5 dataset as baseline and it consists of 2004 annotated images. To our knowledge, this is the first dataset of its kind to be publicly released. The dataset is used to train a deep learning model to classify the labeled images. Evaluated on an independent test set, the model yields an F-1 score of 0.95, indicating that polar lows can be consistently detected from SAR images. Interpretability techniques applied to the deep learning model reveal that atmospheric fronts and cyclonic eyes are key features in the classification. Moreover, experimental results show that the model is accurate even if: (i) such features are significantly cropped due to the limited swath width of the SAR, (ii) the features are partly covered by sea ice and (iii) land is covering significant parts of the images. By evaluating the model performance on multiple input image resolutions (pixel sizes of 500m, 1km and 2km), it is found that higher resolution yield the best performance. This emphasises the potential of using high resolution sensors like SAR for detecting polar lows, as compared to conventionally used sensors such as scatterometers.

Index Terms—Polar lows; Mesocyclones; Deep learning; SAR

I. INTRODUCTION

Polar lows are mesoscale maritime cyclones that form at high latitudes, typically due to cold air outbreaks from sea ice or snow covered regions [1]. They are characterised by rapid development, small scale, strong winds and heavy snowfall. This makes them both difficult to predict and extremely hazardous for maritime activities such as fishing, shipping, petroleum extraction, and offshore wind power production. When making landfall, polar lows are prone to disrupt land and air traffic, destroy infrastructure, and trigger high snow avalanche activity in mountainous regions.

Due to their unpredictable and destructive nature, reliable and precise methods for early detection and tracking of polar lows are desirable. Meteorologists largely rely on direct observations in terms of satellite imagery or numerical weather prediction (NWP) models constrained by observations for detecting polar lows [2]–[9]. In maritime and polar regions, observations almost exclusively originate from satellites. Conventionally, data from scatterometers, radiometers and optical

sensors are assimilated into the NWP models [10], [11]. However, these sensors either rely on sunlight or have a coarse spatial resolution (typically a few to tens of kilometres). Considering that polar lows often occur during the polar night and are small scaled, featuring wind streaks, sharp atmospheric fronts and precipitation cells, observations at higher resolution regardless of light conditions could be beneficial.

Synthetic aperture radars (SARs) are light agnostic and provide imagery at very high spatial resolution (typically a few to tens of metres). Researchers have already indicated that SAR data adds value for monitoring polar lows [12]–[14]. Assimilation of SAR data into NWP models is however challenging, since the exact relationships between radar measurement and geophysical parameters are not trivial, especially at high wind speeds [14]–[16]. An alternative approach to make use of SAR data is to rely on data driven techniques, such as deep learning.

Deep learning has successfully been applied on several remote sensing applications to achieve state of the art results [17]–[20]. Cyclone type phenomena specifically, has been considered in assimilated data [21]–[23], passive microwave data [24], thermal infra-red (IR) data [25]–[29] and scatterometer data [30]. With the exception of [31], deep learning has however been largely overlooked for detecting mesocyclones in SAR data.

This paper investigates the possibility of using deep learning for detecting mesocyclones in general, and polar lows in particular, in SAR images. We aim to answer two main questions: (i) can a deep learning model recognise polar lows in SAR images, and (ii) what significance does the image resolution have on the performance?

To answer these questions, we first show that a training dataset can be constructed from the Sentinel-1 data archive, which is large enough for a deep neural network to be trained. In order to make the dataset large enough, we relax the definition of a polar low to the broader class of mesocyclones. The constructed dataset contains 2004 image samples distributed in two classes: one representing a mesocyclone being present (318 samples) and one representing a normal sea state (1686 samples). In the following, we explain in detail how the dataset is built. To our knowledge, it is the first of its kind to be publicly released.

Then, we show how a deep neural network can be trained on the dataset to perform binary classification with very good performance. The deep learning model and the training procedure is carefully motivated by considering the training dataset size, input image size, and class imbalance. The performance of the model is evaluated for multiple input image resolutions and

*jgra@norceresearch.no

J. Grahn is with NORCE, The Norwegian Research Centre AS

F. M. Bianchi is with the Dept. of Mathematics and Statistics, UiT the Arctic University of Norway and with NORCE, The Norwegian Research Centre AS

interpretability techniques are applied on the model to evaluate what image features are most relevant for the classification.

II. SAR DATASET

This section describes the construction of the dataset for classifying mesocyclones, observed by the Sentinel-1 satellites. The dataset is publicly available¹ and consists of 2004 image samples divided in two classes. The positive class (318 samples) represents mesocyclones and the negative class (1686 samples) represents normal sea states.

A. Positive class: Mesocyclone

A polar low is commonly defined as a small but intense maritime cyclone that forms poleward of the main baroclinic zone [1]. This definition is, however, not precise. In fact, several definitions in terms of geophysical parameters derived either from satellite data or from numerical models have been proposed in the literature [2], [3], [6], [32]–[34].

One of the more recent attempts to quantitatively define polar lows in order to build a climatology, was done by [2]. In particular, different meteorological criteria were investigated in order to classify polar lows in global reanalysis data, concluding that the most effective meteorological parameters were: (i) the difference in sea level pressure (SLP) between the low pressure centre and the surrounding, (ii) the vertical difference in potential temperature between sea surface and the 500 hPa level and (iii) the pole-ward tropopause wind speed. The first criteria implies a certain intensity of the low pressure system. The second criteria is associated to a low static stability of the atmosphere which supports fast intensification by baroclinic instability. The third criteria simply ensures that the system is located poleward of the main baroclinic zone.

In this paper, we consider an approach similar to [2], to find candidate low pressures that are captured by Sentinel-1 SAR satellites. However, to maximise the number of matches, we ignore the last two criteria. In order to still exclude very large scale weather systems, we impose a requirement on the size of the low pressure. Specifically, we consider a depression in the SLP that: (i) is at least 230 Pa lower than the local mean SLP and (ii) does not exceed 200 kilometres in radius. With these criteria, we thus allow for inclusion of mesocyclones that are not necessarily driven by baroclinic instabilities or located in the marine polar air masses.

The selection criteria are applied to the ECMWF reanalysis version 5 (ERA5) dataset, which covers the whole Sentinel-1 data archive (2015-present). The dataset construction process is illustrated in figure 1 and each step is described in detail below.

1) *ERA5 filtering*: The ERA5 dataset [11] consists of hourly reconstructions of a large number of meteorological variables, spanning from 1950 to present. The data can be accessed on a geodetic grid, with a grid spacing of 0.25 degrees horizontally.

Considering the global grid, candidate low pressures were generated by: (i) low-pass filtering the SLP using a 9×9 sliding

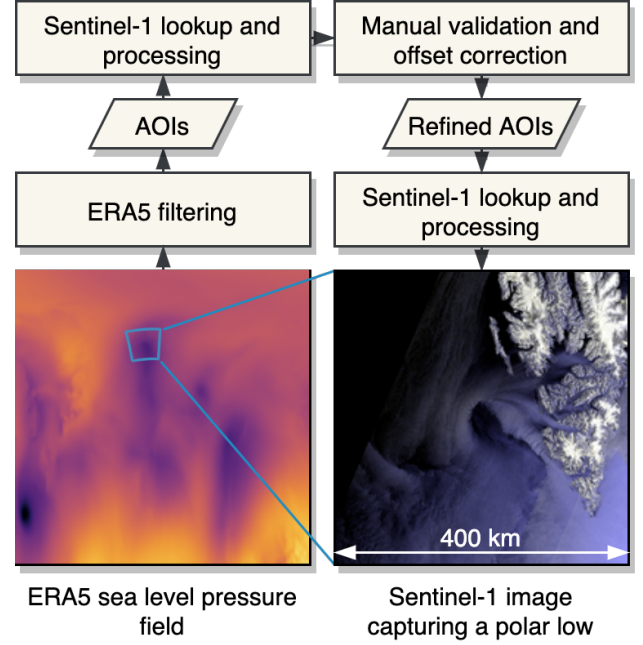


Fig. 1: The dataset construction process illustrated as a flow chart. The starting point is the ERA5 SLP field that is filtered according to our working definition of a polar low to form candidate AOIs. These are used to search for Sentinel-1 data, which is processed (see section II-A2) onto a UTM-grid. The processed images are validated manually and offset corrected by refining the AOIs and reprocessing the images onto a UTM-grid in which the image features are centered.

average filter, (ii) selecting candidate grid cells where the SLP was 230 Pa lower than the low-pass SLP, (iii) grouping adjacent candidate grid cells and (iv) keeping groups with an equivalent radius smaller than 200 km (i.e. with an area less than $200^2\pi$ km²). Each such group was vectorised and constituted a candidate low pressure area of interest (AOI). This filtering process was done on the ERA5 dataset from 1 January 2015 to 31 December 2020 with a time resolution of 3 hours.

The spatial and temporal distributions of candidate AOIs generated from ERA5 and the subsequent matched SAR observations are shown in figure 2. The highest concentrations of candidates were found in the subtropical regions of the North Pacific and North Atlantic. However, due to higher satellite revisit frequencies at higher latitudes, most SAR observations were found in the extra tropical and polar parts of the North Atlantic. Nevertheless, it should be noted that the dataset includes a large portion of mesocyclones that are not strictly polar lows, as defined by e.g. [2].

2) *Sentinel-1 lookup and processing*: For each candidate AOI at time t , we queried the Copernicus Open Access Hub for Sentinel-1 ground range detected (GRD) products in the time interval $t \pm 1.5$ hours. Resulting products were downloaded from Alaska satellite facility (ASF) and processed by: (i) calibrating the data to sigma-nought, (ii) removing thermal noise, (iii) merging orbits of adjacent products, (iv) multi-looking to 500 m resolution in range and azimuth, (v) geocoding to a 400×400 km grid (centered at the AOI) in a universal transverse mercator (UTM) coordinate system with a 500 m

¹To be added.

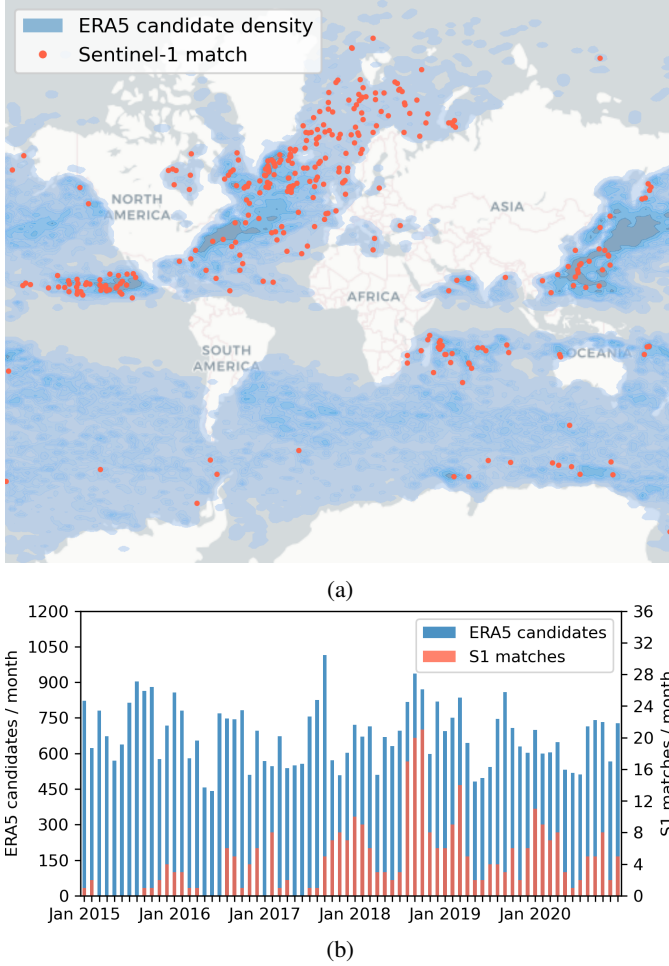


Fig. 2: The spatial distribution of ERA5 candidates and Sentinel-1 matches in (a). The corresponding temporal distribution, as counts per month, in (b). Background map: © OpenStreetMap contributors/CARTO.

grid spacing and (vi) generating red-green-blue (RGB) colour composites.

The RGB colour composites were generated by re-scaling the radar cross-section σ^0 (assumed in decibel scale) to values x ranging from 0 to 1, as:

$$x = \text{clip} \left[\frac{\sigma^0 - a}{b - a} \right]_0^1 \quad (1)$$

where the clipping operation is defined as:

$$\text{clip} [\dots]_q^p = \max(q, \min(\dots, p)) \quad (2)$$

and:

$$a = \text{clip} [\sigma_{2\%}^0]_{-25\text{dB}}^{-15\text{dB}} \quad (3a)$$

$$b = \text{clip} [\sigma_{98\%}^0]_{-10\text{dB}}^{0\text{dB}} \quad (3b)$$

where $\sigma_{2\%}^0$ and $\sigma_{98\%}^0$ are the 2nd and 98th percentiles of σ^0 in the image.

For data with dual polarisation channels, x was used to generate RGB colour composites as:

$$\mathbf{R} = \mathbf{G} = \frac{x_{\parallel} + x_{\times}}{2}, \quad \mathbf{B} = x_{\parallel}$$

where x_{\parallel} and x_{\times} corresponds to the co- and cross-polarised channels, respectively. For single polarisation data, containing only the co-polarised channel, the colour channels were defined as: $\mathbf{R} = \mathbf{G} = \mathbf{B} = x_{\parallel}$. Both dual and single polarisation data were thus considered jointly in the training data set.

3) *Manual validation and offset correction*: Each RGB colour composite was manually validated. Specifically, in each positive image, we asserted the presence of distinctive features (typically an eye or a comma shaped pattern). In general, these features were not centered in the processed images, since the image grid was centered at the candidate AOI originating from ERA5. Therefore, offsets were corrected for by manually centering the AOIs on the eye or comma shaped pattern. The samples were then reprocessed with the refined AOIs.

B. Negative class: Normal sea state

To obtain samples of the negative class, representing a normal sea state, we considered repeat-pass SAR acquisitions successive to those of the positive image samples (i.e. images acquired at the same relative orbit). The motivation of our choice was twofold: (i) Sentinel-1 repeat-passes are separated by at least 6 days, which is enough time for the sea state (and thus the image features) to decorrelate, and (ii) the imaging geometry of repeat-pass acquisitions is nearly identical, such that static/background features appear similar. The second point is important in order to factor out land features from the dataset. Indeed, if the same land features appear in both the positive and negative class, it is expected that a machine learning model will be able to ignore them in the classification task.

As an example, a repeat-pass image set consisting of one positive and eight negative samples is shown in figure 3. To the left, the processed RGB composites are shown. The south tip of Svalbard can be seen statically in all images, while ocean features appear dynamically. The positive sample in the centre, contains a distinct vortex structure. To the right, a map with the footprints of the individual Sentinel-1 products involved is shown, together with the footprint of the image grid. Typically, due to the limited swath of the SAR, the products do not cover the whole image grid across track, leading to missing data in the RGBs in the cross-track direction. Occasionally, some products are not captured, leading to missing data in the along-track direction as well.

The distribution of SLP depression, defined as the difference in SLP (extracted from ERA5) between the image wide average and the average of the centre 100×100 pixels, is shown in figure 4. The positive samples have a strong depression, while the negative samples exhibit a symmetric distribution centred around 0 Pa. This indicate that the negative class, indeed, represents a “normal” sea state not biased towards a low pressure.

In total, 1686 negative sample were generated from the 318 positive ones, resulting in a total of 2004 samples in the dataset. The number of negatives per positive varied depending on the existence of repeat-pass acquisitions, as shown in figure 5. Furthermore, most samples were acquired in the extended wide-swath (EW) mode with two polarisations.

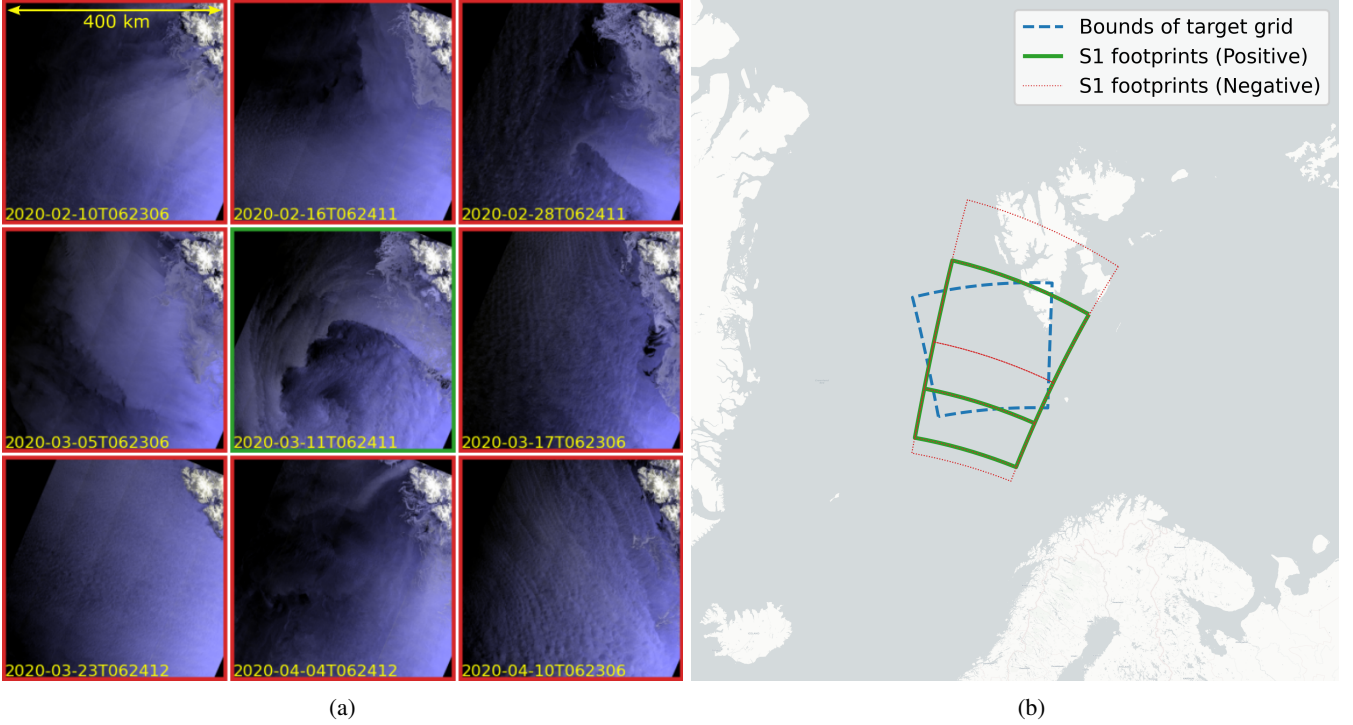


Fig. 3: In (a), a repeat-pass set is shown, consisting of one positive (centre image) and eight negative samples. All samples within a set are processed onto the exact same grid, centered at the low pressure in the positive sample. In (b), the location of the individual products and the grid is displayed. Background map: © OpenStreetMap contributors/CARTO.

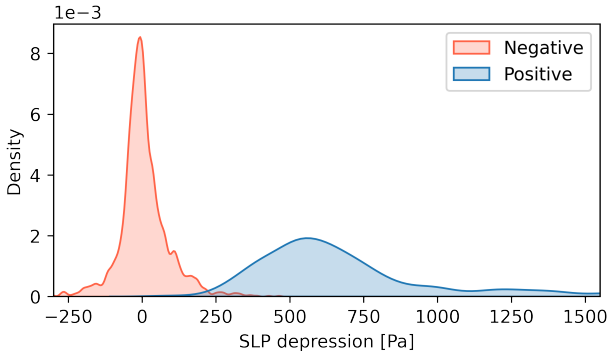


Fig. 4: The distribution of SLP depression for the two classes. The depression is measured as the SLP averaged over the whole image, minus the SLP averaged over the centre 100×100 pixels.

III. DEEP LEARNING

Three immediate challenges can be identified when choosing and training an appropriate deep learning model to perform classification on the dataset: (i) the input image resolution is relatively large, (ii) the training dataset is relatively small, and (iii) the classes are imbalanced. In the following, we discuss how these were dealt with.

A. Deep learning architecture

One of the major benefits of using SAR data, compared to e.g. scatterometer or passive microwave data, is the high image resolution. Although the images in the training dataset were already heavily downsampled from the original resolution of 10-40 m to 500 m, resulting in an image size of 800×800

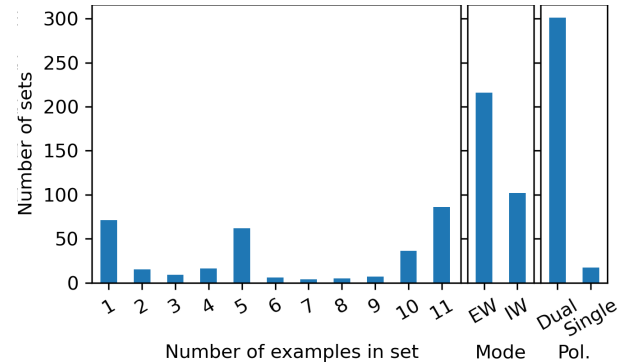


Fig. 5: Overview of the repeat-pass sets, in terms of distributions in size (samples per set), imaging mode and polarisation mode. For each positive sample, we extracted a maximum of 10 negative samples.

pixels, they are relatively large in the context of many popular deep learning models. These are often designed for images of size 256×256 pixels or lower. To preserve details that are specific for the SAR data, such as wind streaks, rain cells or sharp atmospheric fronts, and to enable us to study the added value of high input image resolution, we wish to avoid further downsampling and rather let the model handle the high input image resolution. Convolutional neural networks (CNNs) used for image classification usually consist of a stack of convolutional layers followed by pooling. Each such processing block sequentially increases the feature dimensionality through convolutions, while reducing spatial resolution through pooling. As such, relevant spatial information will gradually become embedded in the feature space. If the input

image is large, the model must either apply an aggressive downsampling in each processing block, or include many blocks and, thus, become very deep. The former can be obtained by large stride in the convolutional and pooling layers, or by using Atrous convolutions [35]. These techniques do, however, come at a cost of discarding spatial information, which we wish to avoid. This leaves us with the option of using a deep architecture, which gradually distill the spatial information and embeds it into the feature space.

Training a very deep network poses two fundamental challenges. Firstly, the gradients of the loss used to update the parameters may gradually vanish as they are backpropagated through the network. Secondly, an architecture with many layers contain many trainable parameters. This makes the model prone to overfitting, unless the training set is exceptionally large, which was not the case in our study.

A solution to address the first problem is to use residual connections, popularized by architectures such as ResNet [36], which facilitate the flow of the gradients during the backpropagation.

Considering the second problem, a ResNet is unfortunately characterized by many trainable parameters. There are, however, more recent deep architectures which include residual connections but have fewer parameters. For example, MobileNet [37] and Xception [38] implement separable 2D convolutions (Sep2DConv), which allows to greatly reduce the number of trainable parameters².

Therefore, we opted for an Xception style architecture, whose details are depicted in figure 6. The entry block consists of a convolutional layer, followed by a batch normalization layer [39] and a ReLU activation function. There are L residual blocks, each one including Sep2DConv layers, batch normalization, ReLU activations and a max-pooling layer. The max-pooling output is combined with the input of the residual block through a skip connection. The convolutional layer in the middle of the skip connection has no activation function and simply applies a kernel of size 1 with stride 2, to match the shape of the input with the one of the output. A global pooling layer reduces the feature map generated by the last residual layer to a single vector, which is processed by the final classifier consisting of a dropout layer [40], a dense layer, and a softmax activation.

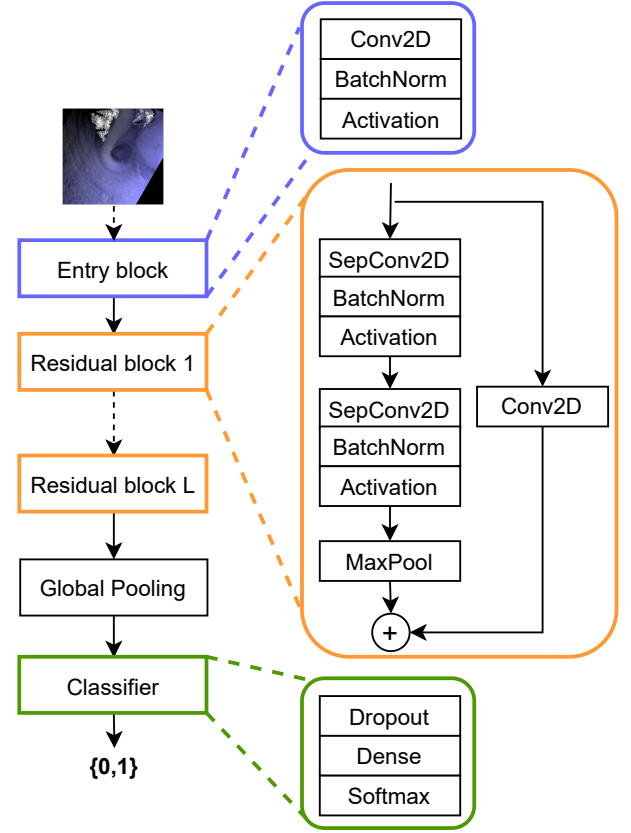


Fig. 6: Architecture details.

Our dataset has been designed by keeping image augmentation in mind. Each low pressure is centered in the image and has a wide area around that can be partially cropped. Each time a new batch of images is fetched inside our deep learning model, the following random transformations are applied on the fly; (i) horizontal and vertical translation (between 0 and 10% of the image size), (ii) horizontal and vertical flip, (iii) rotation (0 to 40 degrees), (iv) zoom (-10% to 10% of the original scale) and finally (v) cropping to the centre 512×512 pixels. Notably, after data augmentation the low pressures are no longer centered in each image. An example of augmented images randomly generated during training is shown in figure 7.

B. Data augmentation

Augmenting the training data by applying random transformation is a common technique used to prevent overfitting. By exposing the deep learning model to perturbations of original inputs, it is possible to improve the robustness of the model. In addition, data augmentation allows to get rid of some bias in the dataset and increase the generalization performance on new unseen data.

²The basic idea behind a Sep2DConv is to replace a matrix of parameters $\mathbf{W} \in \mathbb{R}^{N \times M}$ with an outer product of two unidimensional vectors, $\tilde{\mathbf{W}} = \mathbf{u}^T \otimes \mathbf{v}$, where $\mathbf{u} \in \mathbb{R}^M$ and $\mathbf{v} \in \mathbb{R}^N$, reducing the number of parameters from $M \cdot N$ to $M + N$. This is, actually, a simplification. In practice, a Sep2DConv splits the traditional convolution with a kernel of size $H \times W \times F_{in} \times F_{out}$ with a depth-wise convolution with F_{in} kernels of size $H \times W \times 1$, followed by a point-wise convolution with a kernel of size $1 \times 1 \times F_{out}$.

C. Class imbalance

While the number of positive samples were restricted by the number of matches found on the Sentinel-1 archive, multiple negative samples could be generated for each positive sample. This lead to a natural skewness in the distribution of classes in the dataset: 84% of the samples belong to the negative class and 16% to the positive. We tested and compared three different approaches to train the deep learning model in the presence of class imbalance.

1) *Class-weighting*: We re-weighted the loss function according to class frequencies. Denoting the number of samples in the negative and positive classes respectively by n_0 and n_1 , the loss for samples in the corresponding classes were weighted by $w_0 = \frac{1}{n_0} \frac{n_0+n_1}{2}$ and $w_1 = \frac{1}{n_1} \frac{n_0+n_1}{2}$. This means

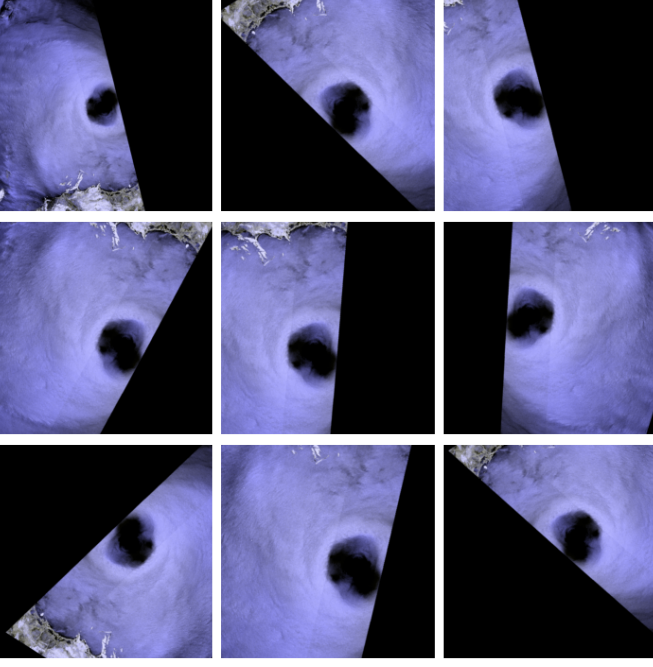


Fig. 7: Examples of random image augmentation. The top-left image is the original.

that each error on the positive class affects the optimization of the model weights to a greater extent.

2) *Oversampling*: We ensured that in each batch there were always the same amount of samples of both classes. Specifically, this was obtained by designating half of the batch to the negative class, and half to the positive. In each epoch, samples from the negative class are seen only once, while samples from the positive class are repeated. We made sure to observe all samples of the negative class at least once during an epoch and to not sample any image twice within a batch.

3) *Rejection sampling*: This strategy drops samples until a balanced distribution across the two classes is obtained. Contrarily to oversampling, each sample is seen at most once in each epoch, which makes the overall training faster.

By empirical comparison, we found that oversampling yields the best performance and, therefore, was the strategy adopted in our experiments.

D. Hyperparameter tuning

To find the optimal configuration of the deep learning model, we searched several hyperparameters and selected those giving the best performance on a validation set. As validation set, we used 10% of the training set. The hyperparameter space and the optimal values found after the optimization procedure are reported in table I. To reduce the hyperparameters space, we only search the number of filters of the first residual blocks and then we double the number in the following blocks.

Since the dataset contains large images and we consider deep models with many parameters, evaluating each hyperparameter configuration is computationally expensive. Therefore, rather than performing an exhaustive search with grid search

Hyperparam.	Search space	Optimal
Activation	{ReLU, SeLU}	ReLU
Conv2D filters	{8, 16}	8
Kernel size	{3, 5}	3
SepConv2D filters	{8, 16, 24, 32}	8
Num. residual blocks	[2, 8]	7
Global pooling	{avg, flat, max}	max
Num. dense layers	[1, 3]	1
Units in the dense layer	{8, 16, 24, 32}	8
Dropout rate	[0.1, 0.6]	0.5
Use batch normalization	{True, False}	True
Learning rate	{1e-2, 1e-3, 1e-4}	1e-3

TABLE I: Hyperparameters space and optimal values found. “Conv2D filters” and “kernel size” refer to the entry block. “Sep-Conv2D filters” refers to the 1st residual block, since the number of filters is double each time in the following blocks.

or evaluating a large number of configurations with a random search, we opted for a more efficient approach. In particular, we used Bayesian hyperparameter optimization [41].

We used a batch size of 16 and the Adam optimizer [42]. During the hyperparameter tuning we trained the model for 50 epochs. After finding the optimal configuration, we trained the final model for 200 epochs.

E. Model interpretability

Due to the presence of many non-linear transformations, it is difficult to interpret the decision process of a neural network and considerable research effort has been devoted to improve our understandings. Gradient based approaches try to find which inputs have the most influence on the model scoring function for a given class [43]–[45]. This is usually done by taking the gradient of the class activation score with respect to each input features [46]. A drawback of gradient based methods is that they give zero contribution to inputs that saturate the ReLU or MaxPool. To capture such shortcomings, a formal notion of explainability was introduced in [47] with the axiom of conservation of total relevance, which states that the sum of relevance of all pixels must match the class score of the model. Specifically, the authors propose to distribute the total relevance of the class score to the input features with Layer-wise Relevance Propagation (LRP). While LRP follows the conservation axiom, it does not specify how to distribute the relevance among the input features. To address this problem DeepLiFT [48] enforces an additional axiom on how to propagate the relevance by following the chain rule.

In this work, we adopt two recent interpretability techniques, that address some of the shortcomings discussed above and are able to provide valuable insights into the decision problem of our model.

1) *Integrated Gradients*: Integrated gradients (IG) [49] has become a popular interpretability technique since it can be applied to any neural network model, is easy to implement, and theoretically grounded. IG aims to satisfy two additional axioms that are not jointly ensured by other existing attribution schemes; (i) if the input and an uninformative baseline differ in exactly one feature, such a feature should be given non-zero attribution, (ii) when two models are functionally equivalent, they must have identical attributions to input features.

Denoting the model scoring function F , the attributions given by IG are

$$\text{IG}(x) := (x - x') \cdot \int_{\alpha=0}^1 \frac{\partial F(x' + \alpha \cdot (x - x'))}{\partial x} d\alpha, \quad (4)$$

where x is a sample in the dataset, x' is the uninformative baseline, and α is an interpolation constant used to perturb the input features.

In our study, we let x' be a black image (all zeros) as the uninformative baseline. As empirically confirmed in our experiments, such a baseline is classified with high confidence to be negative.

Let \mathcal{X} be the set of interpolated images from x' to x . The computation of the integral in (4) is approximated with the sum of the partial derivatives of the images in \mathcal{X} . Figure 8 depicts a small interpolation set \mathcal{X} from the mean-baseline to a positive sample and shows how the classification score changes. By summing the gradients $\frac{\partial F(\mathcal{X})}{\partial x_i}$ one quantifies the

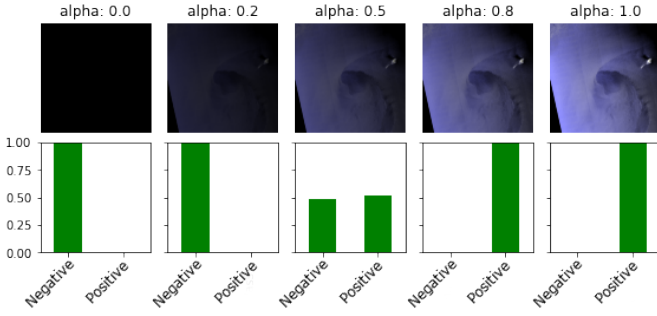


Fig. 8: Top row: linear interpolation from the zero-baseline (left) to an actual sample of positive class (right). Bottom row: classification probabilities assigned by the model at each step of the interpolation.

relationship between the changes in the input features and the changes in the predictions of the model F .

2) *Gradient-weighted Class Activation Mapping*: While IG can be used on any neural network model, gradient-weighted class activation mapping (Grad-CAM) is specific for CNNs. It uses the gradients of a given target class flowing into the final convolutional layer to produce a coarse localization map, which highlights the important regions in the image for predicting the class [50]. We summarize at a high level the main steps of the algorithmic procedure and we refer the interested reader to the original paper for further details: (i) take a trained model and cut it at the k -th layer, which is the layer for which we want to create a Grad-CAM heat-map (usually, the activation after the last convolutional layer), (ii) feed an input image to the complete model and collect the total loss and the output of layer k , (iii) compute the gradients of the output of layer k with respect to the loss, (iv) take parts of the gradient which contribute to the prediction and use to build a heatmap, and (v) resize the heatmap so that it can be overlaid to the original image.

IV. RESULTS

The dataset presented in section II was used to train the model described in section III. Specifically, the dataset was partitioned such that 79% of the samples were used for training

and validation and 21% for testing. Partitioning was done by randomly sampling the repeat-pass sets, such that samples with the same land features were present in both positive and negative samples when training the model (promoting the model to factor these features out as irrelevant to the classification task).

The arguably most attractive property of SAR data, as compared to e.g. scatterometer data, is the high spatial resolution. In order to evaluate the added value of higher spatial resolution, the model accuracy was examined for three different input image resolutions³; 500 m, 1000 m and 2000 m (the latter two obtained by bi-linear down sampling of the first). Hyperparameter tuning was performed for each resolution separately, and the classification performance on the test set is shown in table II. The table displays the mean and standard deviation of true negatives (TNs), false negatives (FNs), false positives (FPs), true positives (TPs) and F1 score obtained from 10 independent runs. It is clear that higher image resolution significantly improves the classification results. In fact, for the highest input resolution, the model is misclassifying on average less than 8 samples (as FN or FP) out of the 435 samples in the test set, with a mean F1 score of 0.94.

Pixel size	TN	FN	FP	TP	F1 score
2km	346.6 \pm 2.1	6.4 \pm 2.1	9.8 \pm 1.9	54.2 \pm 1.9	0.87 \pm 0.01
1km	364.4 \pm 2.1	6.6 \pm 2.1	7.4 \pm 2.1	56.6 \pm 2.1	0.89 \pm 0.02
500m	367.8 \pm 2.7	3.2 \pm 2.7	4.6 \pm 1.7	59.4 \pm 1.7	0.94 \pm 0.01

TABLE II: Classification performance on the test set when using different input resolutions. It is evident that higher input image resolution significantly improves the performance.

TN	FN	FP	TP	F1 score
366	2	5	62	0.95

TABLE III: Classification performance obtained on the specific run where we apply the interpretability techniques.

A model trained on the 500 m resolution images was further examined using the IG and Grad-CAM techniques presented in section III-E. The performance of this specific model is shown in table III and the images it classifies as TPs, FPs, and FNs are discussed in the following.

A. True positives

Of the 62 TP samples (i.e. low pressures correctly classified as low pressures), 4 samples are displayed in figure 9. The first column shows the input RGB colour composites, the second column shows the IG in green and the third column shows the Grad-CAM as a heat map. 3 out of these 4 samples are located in polar regions, while the sample on the second row is an extra-tropical cyclone observed off the coast of Japan. The IG and Grad-CAM overlays indicate that the model is focusing on the cyclonic eye features. The IG overlay has a slightly higher emphasis on the wind fronts as compared to the Grad-CAM. Both the IG and Grad-CAM indicate that the model

³The highest resolution here (500 m) is still considerably lower than the original resolution of the SAR images. However, as discussed in section III-A, the input image size is limited by the depth of the network architecture in relation to the size of the training dataset. Therefore, we did not consider even higher input image resolutions, even if the original data allowed for it.

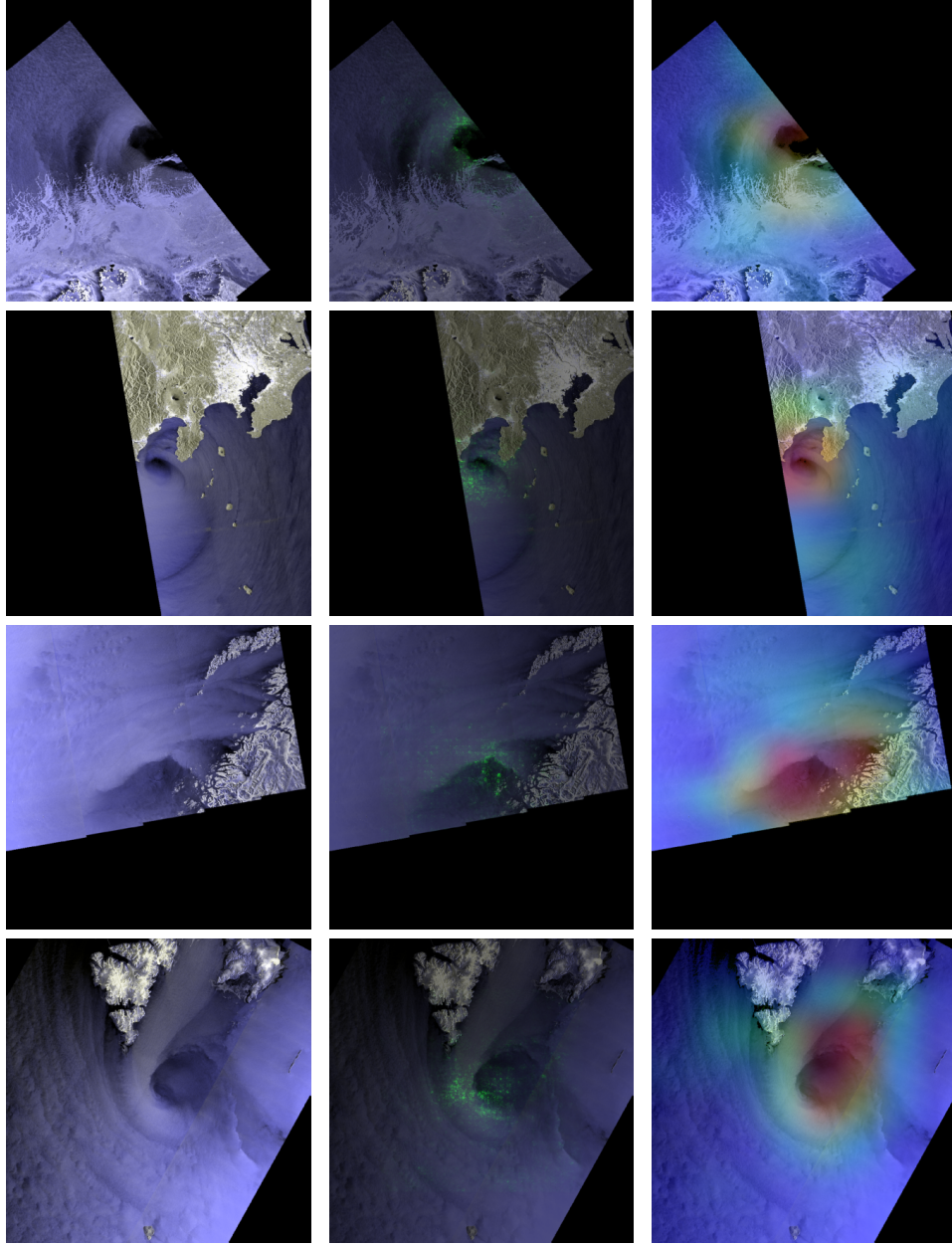


Fig. 9: True positives (4 of 62 samples shown) in first column and corresponding IG and Grad-CAM in the second and third column. The classification scores are 0.99, 0.82, 0.99, and 0.99, respectively.

is effectively disregarding land features as well as the sea ice features appearing in the top row. Notably, in the top row, a large part of the cyclonic eye feature is also cropped due to the limited swath width of the SAR. This is the case in multiple samples classified as TP, indicating a certain robustness to image features being cropped or obscured by e.g. sea ice.

B. False positives

The model classified 5 samples as FP (i.e. normal sea state incorrectly classified as low pressures), of which 4 are shown in figure 10. The top two samples are presumably difficult to classify correctly (or the ground truth label could potentially be wrong), as they actually contain some pronounced wind fronts. Considering the IG and Grad-CAM, indeed the model

is focusing on these wind features. The sample on the third row also contains a pronounced wind front that the model is focusing on, but the front is not curved. The classification score is however only 0.57 for this sample. In the fourth sample, no wind front is visible, but the IG and Grad-CAM reveal that the model focuses on a wind wake (formed behind the Izu peninsula, Japan, located in the image centre), which may be misinterpreted as a cyclonic eye.

C. False negatives

Only two samples of the positive class were incorrectly classified as negatives, i.e. mistaken as normal sea state while being labeled as low pressures. These are shown in figure 11. Here, IG are not computed, since a black image cannot be used

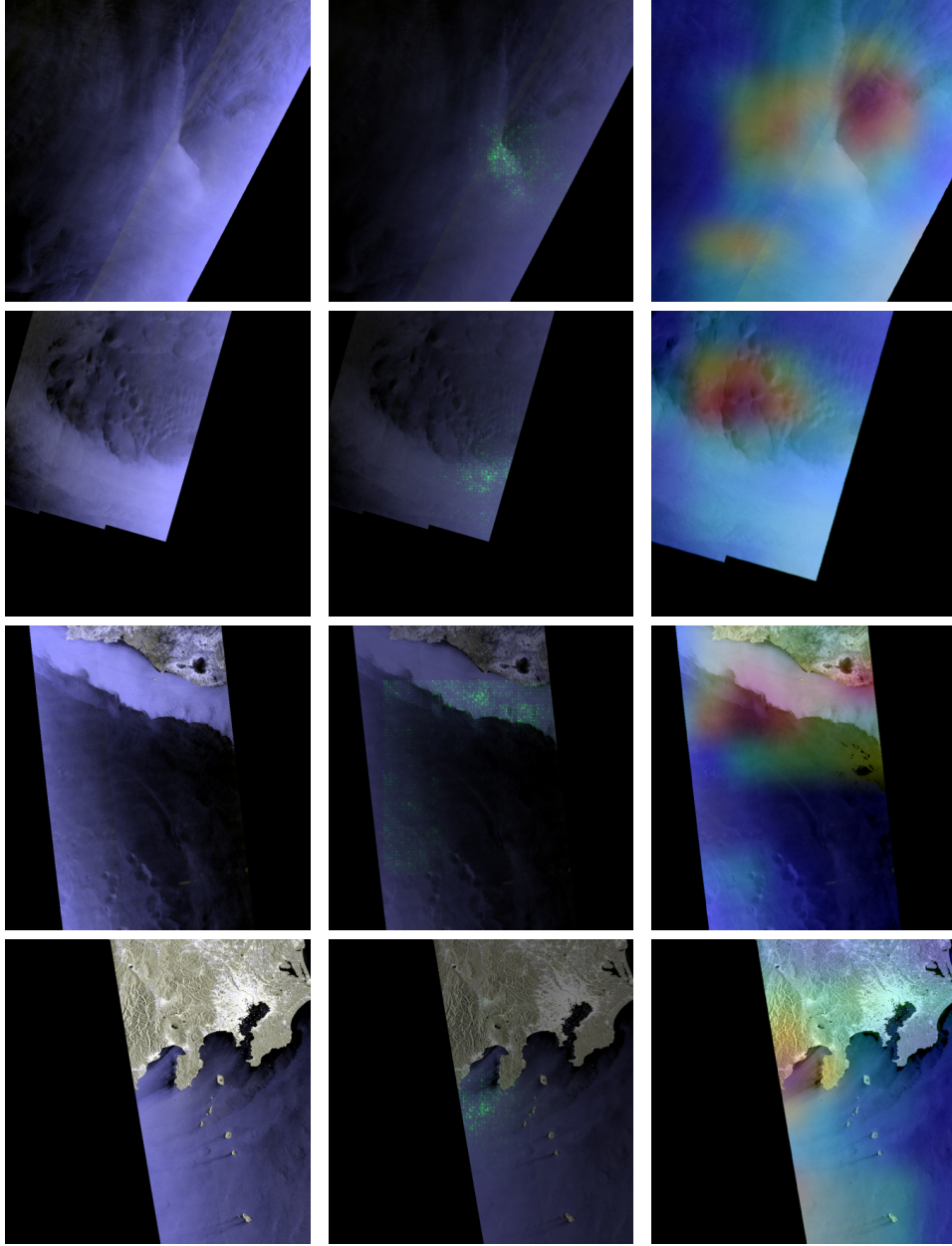


Fig. 10: False positives (4 of 5 samples shown), with classification scores 0.89, 0.92, 0.57 and 0.87.

as a baseline for the negative class. Nevertheless, Grad-CAM can still be computed and is shown in the second column. It can be noted that both images suffer from lacking data due to the limited swath width of the SAR acquisitions. Indeed, the Grad-CAM indicate that the model is not focusing on the darker center features as was the case for the TP samples in figure 9. It should however be emphasised that this happens for only 2 of the 368 negative samples in the test set.

V. CONCLUSIONS

In this study, we show that SAR images from the Sentinel-1 satellites provide an attractive data source for automatic and accurate detection of maritime mesocyclones, such as polar lows. Specifically, we show that sufficiently many image examples can be found to build a labeled dataset for a

deep learning model to be trained. By further comparing our deep learning model when trained on different input image resolutions, we find that higher resolution yields significantly better performance. This highlights the added value of using SAR data, as compared to conventionally used sensors of lower resolution. In particular, at 500 meters resolution we get an F1 score of 0.94, as compared to 0.87 at 2 km resolution (comparable to modern scatterometers).

It should further be noted that the highest resolution tested in this study (500 meters) is primarily limited by the size of the training dataset and not the native resolution of the SAR sensor (10-40 meters). Thus, even higher input image resolutions could in principle be considered, potentially with even better performance. Larger input image sizes, however, ideally require deeper neural network architectures, with more

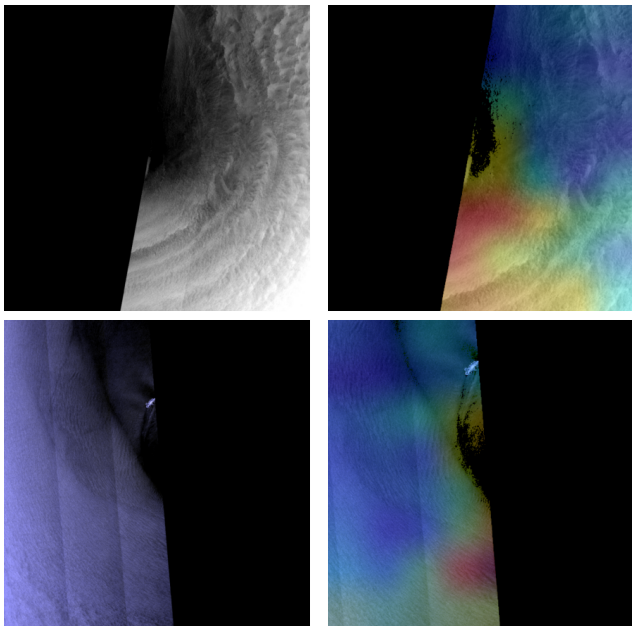


Fig. 11: False Negatives (all samples shown), with classification scores 0.96 and 0.79.

trainable weights, which in turn require larger training datasets to avoid over-fitting. With an increasing amount of SAR data being available however, larger training datasets could be constructed in the future, which may enable even better performance.

By design, the training dataset contains spiral-form low pressures in the positive class. By analyzing IG and Grad-CAM on the trained model, we verify that the spiral shaped atmospheric fronts and the low wind centres yield most of the class attribution. Moreover, we conclude that: (i) these characteristic wind features do not need to be fully covered in the images, but can be substantially cropped due to the limited swath width of the SAR, (ii) wind features can be partly covered by sea ice and still be identified by the model, and (iii) the model is able to ignore land features in the images. The last point can be verified thanks to the procedure used to obtain the negative samples, i.e. through repeat-pass acquisitions (see section II-B).

In summary, we find that the application of deep neural networks on SAR data for recognising maritime mesocyclones in general and polar lows in particular, is promising. Further evaluation and direct comparison to other data from sensors as well as conventional NWP based detection methods is however encouraged.

VI. ACKNOWLEDGMENTS

The authors would like to thank Patrick Stoll for valuable feedback on the manuscript. Thanks to those involved in developing the GDAR software, processing of SAR data was a treat, especially thanks to Heidi Hindberg, Yngvar Larsen and Tom Grydeland. We also want to thank Temesgen Gebrie Yitayew and Hannah Vickers, for help in successful proposal writing. The work was funded by the European space agency

(ESA), under the open call project *Polar low detection based on Sentinel-1 data* (contract number 4000129961).

REFERENCES

- [1] E. A. Rasmussen, "Polar lows," in *A Half Century of Progress in Meteorology: A Tribute to Richard Reed*. Springer, 2003, pp. 61–78.
- [2] P. J. Stoll, R. G. Graversen, G. Noer, and K. Hodges, "An objective global climatology of polar lows based on reanalysis data," *Quarterly Journal of the Royal Meteorological Society*, vol. 144, no. 716, pp. 2099–2117, 2018.
- [3] W. Yanase, H. Niino, I. W. Shun-ichi, K. Hodges, M. Zahn, T. Spengler, and I. A. Gurrich, "Climatology of polar lows over the sea of japan using the jra-55 reanalysis," *Journal of Climate*, vol. 29, no. 2, pp. 419–437, 2016.
- [4] A.-M. Blechschmidt, "A 2-year climatology of polar low events over the nordic seas from satellite remote sensing," *Geophysical Research Letters*, vol. 35, no. 9, 2008.
- [5] K. Wilhelmssen, "Climatological study of gale-producing polar lows near norway," *Tellus A: Dynamic Meteorology and Oceanography*, vol. 37, no. 5, pp. 451–459, 1985.
- [6] G. Zappa, L. Shaffrey, and K. Hodges, "Can polar lows be objectively identified and tracked in the ecmwf operational analysis and the era-interim reanalysis?" *Monthly Weather Review*, vol. 142, no. 8, pp. 2596–2608, 2014.
- [7] C. Michel, A. Terpstra, and T. Spengler, "Polar mesoscale cyclone climatology for the nordic seas based on era-interim," *Journal of Climate*, vol. 31, no. 6, pp. 2511–2532, 2018.
- [8] L. Xia, M. Zahn, K. Hodges, F. Feser, and H. Storch, "A comparison of two identification and tracking methods for polar lows," *Tellus A: Dynamic Meteorology and Oceanography*, vol. 64, no. 1, p. 17196, 2012.
- [9] P. J. Stoll, T. Spengler, A. Terpstra, and R. G. Graversen, "Polar lows – moist-baroclinic cyclones developing in four different vertical wind shear environments," *Weather and Climate Dynamics*, vol. 2, no. 1, pp. 19–36, 2021.
- [10] M. Muller, M. Homleid, K.-I. Ivarsson, M. A. Ø. Koltzow, M. Lindskog, K. H. Midtbø, U. Andrae, T. Aspelien, L. Berggren, D. Bjørge, P. Dahlgren, J. Kristiansen, R. Randriamampianina, M. Ridal, and O. Vignes, "Arome-metcoop: A nordic convective-scale operational weather prediction model," *Weather and Forecasting*, vol. 32, no. 2, pp. 609 – 627, 2017.
- [11] H. Hersbach, B. Bell, P. Berrisford, S. Hirahara, A. Horányi, J. Muñoz-Sabater, J. Nicolas, C. Peubey, R. Radu, D. Schepers *et al.*, "The era5 global reanalysis," *Quarterly Journal of the Royal Meteorological Society*, vol. 146, no. 730, pp. 1999–2049, 2020.
- [12] G. W. K. Moore and P. W. Vachon, "A polar low over The Labrador Sea: Interactions with topography and an upper-level potential vorticity anomaly, and an observation by RADARSAT-1 SAR," *Geophysical research letters*, vol. 29, no. 16, p. 1773, Aug. 2002.
- [13] B. R. Furevik, H. Schyberg, G. Noer, F. Tvetter, and J. Röhrs, "Asar and ascot in polar low situations," *Journal of Atmospheric and Oceanic Technology*, vol. 32, no. 4, pp. 783–792, 2015.
- [14] M. Tollinger, R. Graversen, and H. Johnsen, "High-resolution polar low winds obtained from unsupervised sar wind retrieval," *Remote Sensing*, vol. 13, no. 22, p. 4655, 2021.
- [15] B. Chapron, H. Johnsen, and R. Garello, "Wave and wind retrieval from sar images of the ocean," in *Annales des telecommunications*, vol. 56, no. 11. Springer, 2001, pp. 682–699.
- [16] A. A. Mouche, F. Collard, B. Chapron, K.-F. Dagestad, G. Guitton, J. A. Johannessen, V. Kerbaol, and M. W. Hansen, "On the use of doppler shift for sea surface wind retrieval from sar," *IEEE Transactions on Geoscience and Remote Sensing*, vol. 50, no. 7, pp. 2901–2909, 2012.
- [17] X. X. Zhu, D. Tuia, L. Mou, G.-S. Xia, L. Zhang, F. Xu, and F. Fraundorfer, "Deep learning in remote sensing: A comprehensive review and list of resources," *IEEE Geoscience and Remote Sensing Magazine*, vol. 5, no. 4, pp. 8–36, 2017.
- [18] F. M. Bianchi, M. M. Espeseth, and N. Borch, "Large-scale detection and categorization of oil spills from sar images with deep learning," *Remote Sensing*, vol. 12, no. 14, p. 2260, 2020.
- [19] F. M. Bianchi, J. Grahm, M. Eckerstorfer, E. Malnes, and H. Vickers, "Snow avalanche segmentation in sar images with fully convolutional neural networks," *IEEE Journal of Selected Topics in Applied Earth Observations and Remote Sensing*, vol. 14, pp. 75–82, 2020.
- [20] L. T. Luppino, M. Kampffmeyer, F. M. Bianchi, G. Moser, S. B. Serpico, R. Jenssen, and S. N. Anfinsen, "Deep image translation with an affinity-based change prior for unsupervised multimodal change detection," *IEEE Transactions on Geoscience and Remote Sensing*, 2021.

- [21] Y. Liu, E. Racah, J. Correa, A. Khosrowshahi, D. Lavers, K. Kunkel, M. Wehner, W. Collins *et al.*, "Application of deep convolutional neural networks for detecting extreme weather in climate datasets," *arXiv preprint arXiv:1605.01156*, 2016.
- [22] D. Matsuoka, M. Nakano, D. Sugiyama, and S. Uchida, "Deep learning approach for detecting tropical cyclones and their precursors in the simulation by a cloud-resolving global nonhydrostatic atmospheric model," *Progress in Earth and Planetary Science*, vol. 5, no. 1, pp. 1–16, 2018.
- [23] S. Giffard-Roisin, M. Yang, G. Charpiat, C. Kumler Bonfanti, B. Kégl, and C. Monteleoni, "Tropical cyclone track forecasting using fused deep learning from aligned reanalysis data," *Frontiers in Big Data*, vol. 3, p. 1, 2020.
- [24] A. Wimmers, C. Velden, and J. H. Cossuth, "Using deep learning to estimate tropical cyclone intensity from satellite passive microwave imagery," *Monthly Weather Review*, vol. 147, no. 6, pp. 2261–2282, 2019.
- [25] P. Golubkin, J. Smirnova, and L. Bobylev, "Satellite-derived spatiotemporal distribution and parameters of north atlantic polar lows for 2015–2017," *Atmosphere*, vol. 12, no. 2, 2021.
- [26] C. Kumler-Bonfanti, J. Stewart, D. Hall, and M. Govett, "Tropical and extratropical cyclone detection using deep learning," *Journal of Applied Meteorology and Climatology*, vol. 59, no. 12, pp. 1971–1985, 2020.
- [27] B.-F. Chen, B. Chen, H.-T. Lin, and R. L. Elsberry, "Estimating tropical cyclone intensity by satellite imagery utilizing convolutional neural networks," *Weather and Forecasting*, vol. 34, no. 2, pp. 447–465, 2019.
- [28] R. Pradhan, R. S. Aygun, M. Maskey, R. Ramachandran, and D. J. Cecil, "Tropical cyclone intensity estimation using a deep convolutional neural network," *IEEE Transactions on Image Processing*, vol. 27, no. 2, pp. 692–702, 2017.
- [29] M. Krinitskiy, P. Verezemskaya, K. Grashchenkov, N. Tilinina, S. Gulev, and M. Lazzara, "Deep convolutional neural networks capabilities for binary classification of polar mesocyclones in satellite mosaics," *Atmosphere*, vol. 9, no. 11, p. 426, 2018.
- [30] M. Xie, Y. Li, and K. Cao, "Global cyclone and anticyclone detection model based on remotely sensed wind field and deep learning," *Remote Sensing*, vol. 12, no. 19, p. 3111, 2020.
- [31] A. R. Carmo, N. Longépé, A. Mouche, D. Amorosi, and N. Cremer, "Deep learning approach for tropical cyclones classification based on c-band sentinel-1 sar images," in *2021 IEEE International Geoscience and Remote Sensing Symposium IGARSS*. IEEE, 2021, pp. 3010–3013.
- [32] T. J. Bracegirdle and S. L. Gray, "An objective climatology of the dynamical forcing of polar lows in the nordic seas," *International Journal of Climatology: A Journal of the Royal Meteorological Society*, vol. 28, no. 14, pp. 1903–1919, 2008.
- [33] G. Noer, Ø. Saetra, T. Lien, and Y. Gusdal, "A climatological study of polar lows in the nordic seas," *Quarterly Journal of the Royal Meteorological Society*, vol. 137, no. 660, pp. 1762–1772, 2011.
- [34] J. E. Smirnova, P. A. Golubkin, L. P. Bobylev, E. V. Zabolotskikh, and B. Chapron, "Polar low climatology over the nordic and barents seas based on satellite passive microwave data," *Geophysical Research Letters*, vol. 42, no. 13, pp. 5603–5609, 2015.
- [35] L.-C. Chen, G. Papandreou, I. Kokkinos, K. Murphy, and A. L. Yuille, "Deeplab: Semantic image segmentation with deep convolutional nets, atrous convolution, and fully connected crfs," *IEEE transactions on pattern analysis and machine intelligence*, vol. 40, no. 4, pp. 834–848, 2017.
- [36] C. Szegedy, S. Ioffe, V. Vanhoucke, and A. A. Alemi, "Inception-v4, inception-resnet and the impact of residual connections on learning," in *Thirty-first AAAI conference on artificial intelligence*, 2017, pp. 1251–1258.
- [37] A. G. Howard, M. Zhu, B. Chen, D. Kalenichenko, W. Wang, T. Weyand, M. Andreetto, and H. Adam, "Mobilenets: Efficient convolutional neural networks for mobile vision applications," *arXiv preprint arXiv:1704.04861*, 2017.
- [38] F. Chollet, "Xception: Deep learning with depthwise separable convolutions," in *Proceedings of the IEEE conference on computer vision and pattern recognition*, 2017, pp. 1251–1258.
- [39] S. Ioffe and C. Szegedy, "Batch normalization: Accelerating deep network training by reducing internal covariate shift," in *International conference on machine learning*. PMLR, 2015, pp. 448–456.
- [40] N. Srivastava, G. Hinton, A. Krizhevsky, I. Sutskever, and R. Salakhutdinov, "Dropout: a simple way to prevent neural networks from overfitting," *The journal of machine learning research*, vol. 15, no. 1, pp. 1929–1958, 2014.
- [41] J. Snoek, H. Larochelle, and R. P. Adams, "Practical bayesian optimization of machine learning algorithms," *Advances in neural information processing systems*, vol. 25, 2012.
- [42] D. P. Kingma and J. Ba, "Adam: A method for stochastic optimization," *International Conference on Learning Representations*, 2014.
- [43] D. Smilkov, N. Thorat, B. Kim, F. Viégas, and M. Wattenberg, "Smoothgrad: removing noise by adding noise," *International Conference on Machine Learning*, 2017.
- [44] M. D. Zeiler and R. Fergus, "Visualizing and understanding convolutional networks," in *European conference on computer vision*. Springer, 2014, pp. 818–833.
- [45] J. T. Springenberg, A. Dosovitskiy, T. Brox, and M. Riedmiller, "Striving for simplicity: The all convolutional net," *International Conference on Learning Representations*, 2015.
- [46] K. Simonyan, A. Vedaldi, and A. Zisserman, "Deep inside convolutional networks: Visualising image classification models and saliency maps," *International Conference on Learning Representations*, 2014.
- [47] S. Bach, A. Binder, G. Montavon, F. Klauschen, K.-R. Müller, and W. Samek, "On pixel-wise explanations for non-linear classifier decisions by layer-wise relevance propagation," *PloS one*, vol. 10, no. 7, p. e0130140, 2015.
- [48] A. Shrikumar, P. Greenside, and A. Kundaje, "Learning important features through propagating activation differences," in *International Conference on Machine Learning*. PMLR, 2017, pp. 3145–3153.
- [49] M. Sundararajan, A. Taly, and Q. Yan, "Axiomatic attribution for deep networks," in *International Conference on Machine Learning*. PMLR, 2017, pp. 3319–3328.
- [50] R. R. Selvaraju, M. Cogswell, A. Das, R. Vedantam, D. Parikh, and D. Batra, "Grad-cam: Visual explanations from deep networks via gradient-based localization," in *Proceedings of the IEEE international conference on computer vision*, 2017, pp. 618–626.